Spatial metastability control via compositional heterostructures for enhanced TRIP behavior in ferrous medium-entropy alloys

Sujung Son[a,*], Hyojeong Ha[a], Soo Vin Ha[a], Ji-Su Lee[a], Shi Woo Lee[a], Bon Woo Koo[a], Zhe Gao[b], Jae-il Jang[b], Byeong-Joo Lee[a], Hyoung Seop Kim[a,c,d,*]

[a] *Department of Materials Science and Engineering, Pohang University of Science and Technology (POSTECH), Pohang, 37673, Republic of Korea*

[b] *Division of Materials Science and Engineering, Hanyang University, Seoul 04763, Republic of Korea*

[c] *Graduate Institute of Ferrous and Energy Materials Technology, Pohang University of Science and Technology (POSTECH), Pohang, 37673, Republic of Korea*

[d] *Advanced Institute for Materials Research (WPI-AIMR), Tohoku University, Sendai 980-8577, Japan*

*Corresponding authors: Prof. Hyoung Seop Kim, Graduate Institute of Ferrous and Energy Materials Technology, Pohang University of Science and Technology (POSTECH), Pohang, 37673, Republic of Korea, E-mail: hskim@postech.ac.kr; Dr. Sujung Son, Department of Materials Science and Engineering, Pohang University of Science and Technology (POSTECH), Pohang, 37673, Republic of Korea, E-mail: sjson@postech.ac.kr

Abstract

This study introduces a novel multi-material design strategy termed spatial metastability control (SMC) for enhancing the transformation-induced plasticity (TRIP) behaviors in ferrous medium-entropy alloys (MEAs). The approach utilizes a compositional heterostructure by integrating pure Fe into a metastable MEA, establishing a gradual phase stability across the MEA/Fe interface. This gradient forms a distinct transition region characterized by refined grain size, thermal martensite formation, and moderate solid solution strengthening. The engineered spatial distribution of metastability facilitates efficient strain accommodation and promotes sequential TRIP activation. As a result, the SMC-designed alloys demonstrate exceptional strength-ductility synergies at both room and cryogenic temperatures. The SMC30 sample exhibits extensive martensitic transformation (~95 vol%), validating the effectiveness of spatially engineered phase metastability in enhancing TRIP behavior. This design framework offers a versatile pathway for developing next-generation structural alloys with tunable mechanical performance through spatial control of phase stability across a broad temperature range.

Keywords: Heterostructures; Spatial metastability control; Severe plastic deformation; Mechanical properties; Transformation-induced plasticity

1. Introduction

Heterostructures have emerged as a highly effective design strategy for enhancing the mechanical properties of structural materials, simultaneously achieving superior strength and ductility by integrating domains with distinct microstructural features, such as chemical composition, grain size, and crystal structure [1-3]. While each domain within a heterostructured material individually exhibits characteristic mechanical behavior, the combination of these domains often results in synergistic properties that surpass the rule-of-mixtures prediction based on the constituent phases alone [4-7].

Recently, metastable high-entropy alloys (HEAs) and medium-entropy alloys (MEAs) have garnered significant attention due to their exceptional strain-hardening capability mediated by transformation-induced plasticity (TRIP) [8-10]. Enhanced strain hardening in these TRIP-based alloys originates primarily from dynamic Hall-Petch strengthening and efficient dislocation accumulation enabled by multi-phase microstructures. Despite the promising advancements in TRIP HEAs and MEAs, there remains a critical demand for incorporating additional strengthening approaches. In this context, heterostructuring has become increasingly prominent, demonstrating substantial improvements in mechanical properties across various HEA and MEA systems [4, 11-14] .

To further maximize the mechanical performance of TRIP alloys, recent efforts have attempted to combine metastability with heterostructuring, aiming to exploit both phase transformation and strain partitioning mechanisms synergistically. However, conventional heterostructuring typically involves adjusting the volume fraction of hard and soft domains, with limited focus on precise metastability tuning within or between the domains. Furthermore, conventional stable domains may inadvertently suppress TRIP behavior in adjacent metastable domains due to chemical intermixing [15].

To overcome these limitations, this study proposes an innovative alloy design strategy, termed spatial metastability control (SMC), specifically tailored for ferrous MEA systems. Because the Fe content critically influences metastability in ferrous MEAs [8, 16], the deliberate integration of pure Fe into a metastable ferrous MEA provides compositional and structural continuity. However, pure Fe itself exhibits limited strength and strain-hardening capacity due to insufficient solid solution strengthening and a lack of TRIP/TWIP mechanisms [17]. Therefore, combining Fe with a metastable MEA within a multi-material system is expected to create complementary properties by enhancing TRIP activity within the MEA matrix while strengthening the Fe-rich region.

By incorporating pure Fe into a metastable ferrous MEA matrix, an intermediate "transition region" inevitably forms between MEA and Fe due to thermal and mechanical mixing [18, 19]. In transition region, compositional gradients are formed at the interfaces where the metastability of the face-centered cubic (FCC) phase is finely and spatially tuned. Such precise spatial modulation of metastability facilitates sequential and extensive TRIP activation throughout the structure, both at room and cryogenic temperatures.

Spatially controlling phase stability via compositional gradients shifts the focus from phase contrast to metastability contrast, offering a more effective strategy for activating and guiding TRIP in heterostructured alloys. This approach enables exceptional strength-ductility combinations and provides valuable insights for designing spatially architected structural materials.

2. Materials and methods

Three distinct powder mixtures were prepared by varying the contents of pure Fe metal powder (10, 30, and 50 at%) added to a metastable ferrous MEA ($Fe_{60}Co_{15}Cr_{10}Ni_{15}$, at%) powder. Hereafter, these multi-material systems incorporating 10, 30, and 50 at% pure Fe are denoted as SMC10, SMC30, and SMC50, respectively. All powder mixtures were pre-compacted into disk-shaped samples (10 mm diameter and 1.5 mm thickness) using a manual press under an applied pressure of 40 MPa. The pre-compacted disks were subsequently processed by high-pressure torsion (HPT) at a pressure of 5 GPa for four revolutions at a rotation speed of 1 rpm. To facilitate recovery and recrystallization, the HPT-processed samples were annealed at 800 °C for 10 minutes. For reference, single-phase ferrous MEA samples without pure Fe additions were fabricated using identical processing conditions.

To predict the equilibrium phase diagram and calculate the Gibbs free energy difference between the BCC and FCC phases ($\Delta G^{FCC\rightarrow BCC}$) as a function of Fe content in the ferrous MEA, thermodynamic calculations were performed using Thermo-Calc software.

Specimens for microstructural characterization were initially prepared by mechanical polishing, followed by electropolishing. The crystal structures of the constituent phases were identified via X-ray diffraction (XRD; Bruker D8 Advance) using Cu Kα radiation at a scan rate of 2° per minute. Phase morphologies and chemical compositions were investigated using field-emission scanning electron microscopy (FE-SEM; JEOL JSM-7100F and XL30S FEG) equipped with backscattered electron (BSE), electron backscatter diffraction (EBSD), and energy dispersive spectroscopy (EDS) detectors. The density of these alloys was examined by the Archimedes method.

Mechanical properties of the alloys were evaluated by nanoindentation tests and uniaxial tensile tests at room temperature (298 K) and cryogenic temperature (77 K). The nanoindentation experiments were conducted on specific regions using the Nanoindenter- XP equipped with a Berkovich tip. Peak loads (P_{max}) of 20 mN and constant indentation strain rate of 0.05 s^{-1} were employed. Continuous stiffness measurement (CSM) mode was utilized to obtain hardness values. The tensile tests were performed on dog-bone-shaped specimens with gauge dimensions of 1.5 mm length, 1.0 mm width, and 0.8 mm thickness using a universal testing machine (Instron 8862 and US/SSTM) at a quasi-static strain rate of 10^{-3} s^{-1}. At 298 K, strain measurements were precisely captured using a digital image correlation (DIC) system (ARAMIS 12M). At 77 K, specimen elongation was determined by measuring displacement between pre-indented gauge marks before and after tensile deformation. Post-deformation microstructures and fracture surfaces of tested specimens were subsequently analyzed using FE-SEM.

3. Results & discussion

The thermodynamic calculations in Fig. 1 were performed to elucidate the local metastability of the transition region with a unique and previously unexplored intermediate chemical composition between MEA and Fe. The equilibrium phase diagram (Fig. 1a) indicates that with increasing Fe content, the FCC region contracts, whereas the FCC+BCC and single BCC phase regions expand. At the annealing temperature of 1073 K, compositions above ~90 at.% Fe are expected to form FCC+BCC dual phases, transitioning to a single BCC phase at Fe contents exceeding ~96 at%.

Gibbs free energy difference $\Delta G^{FCC\rightarrow BCC}$ calculations (Fig. 1b) at room temperature (298 K) and annealing temperature (1073 K) illustrate significantly reduced FCC stability with increasing Fe content. This thermodynamic insight clearly delineates three distinct regions: (1) a metastable FCC-dominated MEA region, (2) a stable BCC-rich Fe region, and (3) a metastability gradient "transition region" at the interface. Therefore, powder mixtures containing varying Fe fractions (SMC10, SMC30, and SMC50) were prepared to systematically explore these effects.

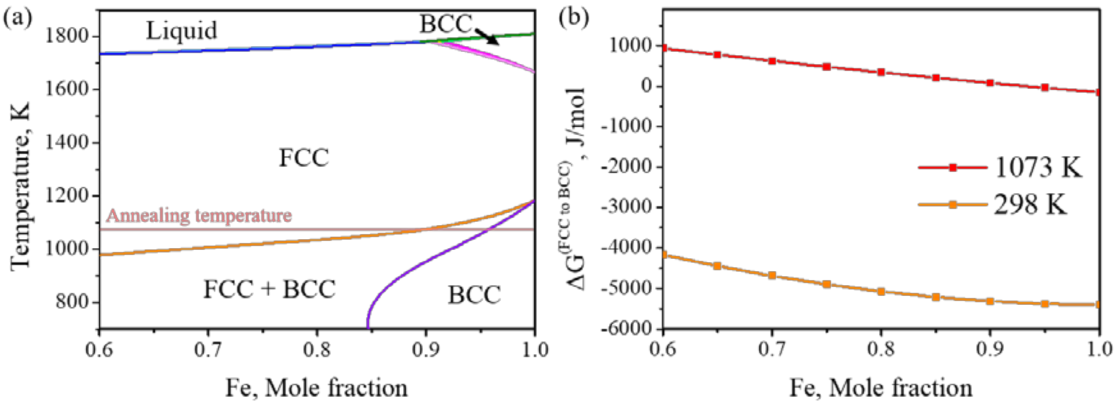

Figure 1. Thermodynamic calculation of ferrous MEA-pure Fe multi-material. (a) Equilibrium phase diagram in a FeCoCrNi alloy system according to the Fe fraction from 0.6 to 1.0. The horizontal line in equilibrium phase diagram indicates the annealing temperature of 1073 K. (b) Calculation of $\Delta G^{FCC\rightarrow BCC}$ at room (298 K) and annealing temperature (1073 K).

SMC10, SMC30, and SMC50 with varying volume fractions of constituent regions were fabricated via powder mixing followed by cold consolidation using the HPT process. The initial powder characteristics are provided in Supplementary Fig. S1. Both powders exhibit similar particle sizes of ~50 μm. The pure Fe powder is single-phase BCC, while the ferrous MEA powder consists mainly of an FCC phase with a minor BCC peak detectable by XRD diffractions.

Fig. 2 presents the cross-sectional microstructures of the cold consolidated disks. As the Fe content increases from SMC10 to SMC50, the Fe-rich regions become increasingly prominent, reaching an approximately 1:1 volume ratio in SMC50. The overall compositions derived from each EDS map are summarized in Table 1. The Fe content increases from the initial 59.5 at% in ferrous MEA to 77.2 at% in SMC50, while the concentrations of Co, Cr, and Ni decrease proportionally. In Fig. 2b-d, the Fe and MEA regions in all SMC samples are elongated perpendicular to the compression axis and horizontal to the torsional directions of the HPT process. In SMC10 and SMC30 (Fig. 2b, c), the severe frictional stress during HPT process results in strong interfacial bonding between the constituent powders, producing defect-free bulk samples [20]. In contrast, SMC50 (Fig. 2d) exhibits internal pores, because SMC50 possesses higher volume fraction of hard Fe powder hindering a sound consolidation. The porosity of SMC50 measured by the Archimedes method was 3.8%, which is significantly higher than that of SMC10 (2.0%) and SMC30 (2.1%).

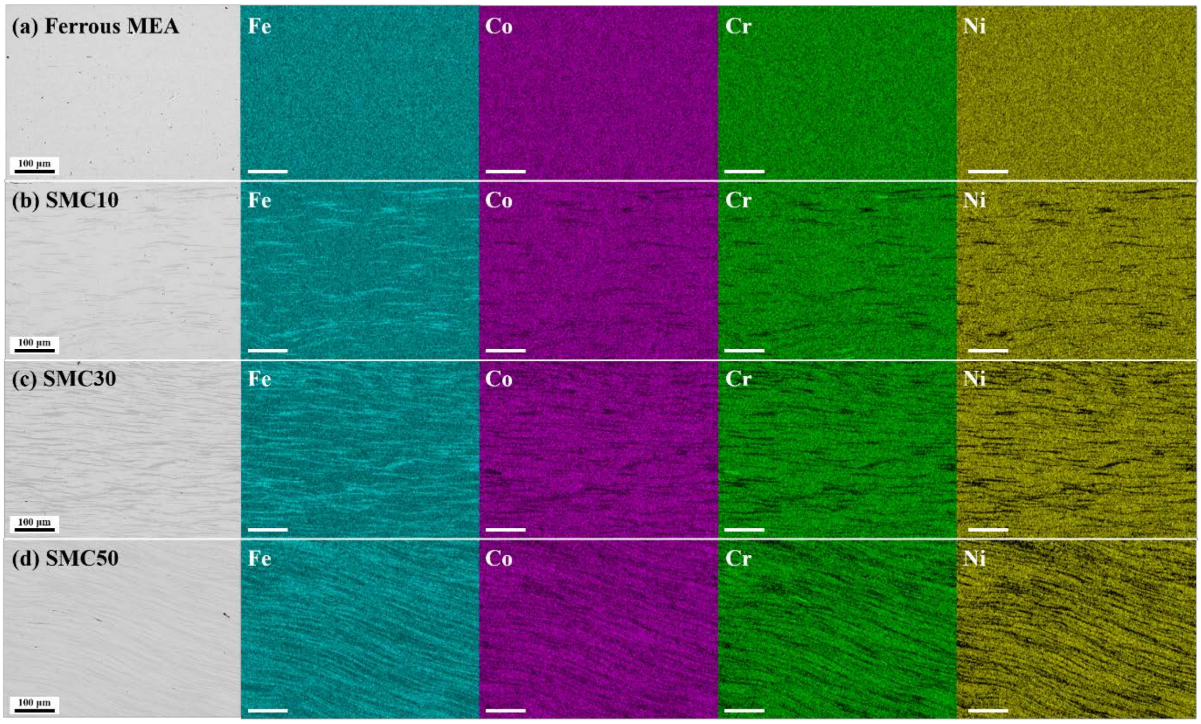

Figure 2. The cross-section BSE images with corresponding EDS maps of (a) ferrous MEA, (b) SMC10, (c) SMC30, and (d) SMC50 after HPT process.

Table 1. Chemical compositions of ferrous MEA and SMC samples.

at%	Co	Cr	Fe	Ni
Ferrous MEA	~14.8	~10.4	~59.5	~15.4

SMC10	~13.5	~9.3	~63.4	~13.8
SMC30	~11.1	~7.7	~69.6	~11.5
SMC50	~8.3	~5.8	~77.2	~8.6

To further analyze the transition region, an EDS line profile was obtained across the MEA and Fe regions in the SMC10 sample (Fig. 3). The line profile reveals repeating MEA and Fe regions, with compositional gradients at their interfaces. During the HPT process, intense shear strain generates random waves, folds, and vortices, promoting intermixing between adjacent regions [21, 22]. This type of mechanical mixing has been reported to produce solid-solution alloying in high-entropy alloys [23], Al-Cu systems [24], and even supersaturated solutions in immiscible alloys [25]. Consequently, the transition region, defined by the compositional overlap between the two phases, exhibited a width of ~1 μm. Additionally, the Fe-rich regions consistently maintain Fe concentrations above 90 at%, indicating that the pure Fe region largely preserves its original chemical configuration despite mechanical processing.

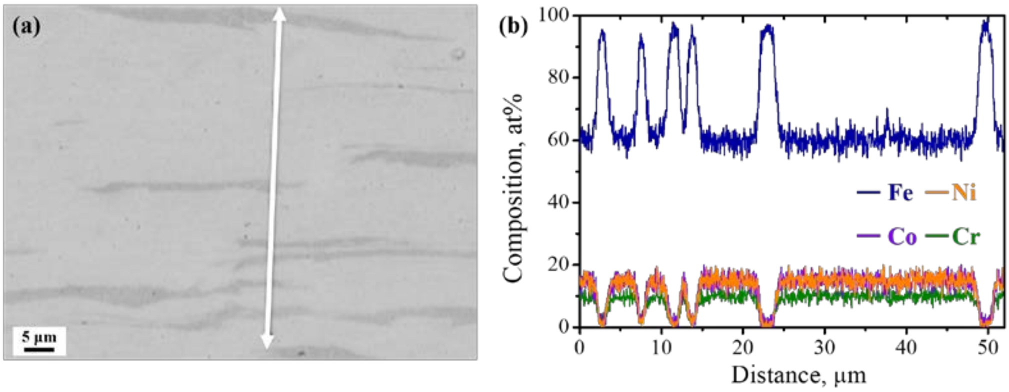

Figure 3. (a) Cross-section SEM image of SMC10 sample and (b) EDS line profiles obtained from the white line indicated in (a).

As-HPT samples are known to exhibit limited ductility due to severe plastic deformation and the high residual dislocations density [26]. To optimize the mechanical properties, annealing process was subjected to as-HPT samples. In the as-HPT samples (supplementary Fig. S2), the microstructures of all samples are predominantly composed of BCC phases due to the severe deformation introduced by HPT process. However, the XRD pattern after annealing (Fig. 4) exhibits a reverse transformation in the ferrous MEA based on the strong FCC peaks. Similar reverse transformations are observed in the SMC samples, where FCC peaks reappear after annealing. However, as the volume fractions of the MEA regions decrease from SMC10 to SMC50, a gradual decrease in FCC peak intensity and a corresponding increase in BCC peak intensity are observed. Interestingly, despite containing only 30 and 50 at% Fe, SMC30 and SMC50 exhibit strong BCC peak intensities that surpass those of the FCC phase. This abnormal phase evolution is attributed by the transition region, which may promote BCC phase formation beyond the BCC volume fraction expected from the nominal Fe content alone.

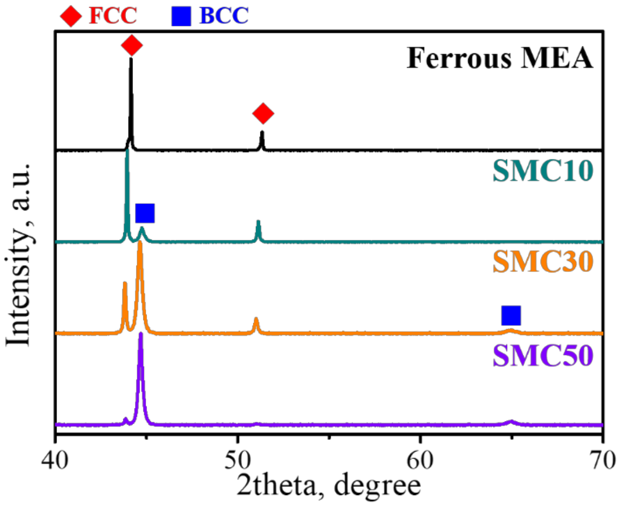

Figure 4. X-ray diffraction patterns of the annealed SMC samples.

To further verify the influence of the transition region to the annealed samples, SEM-BSE images accompanied by EDS elemental maps were displayed in Fig. 5. For comparison, the annealed single-phase ferrous MEA sample without SMC heterostructuring is shown in supplementary Fig. S3. It exhibits a fully recrystallized microstructure composed of equiaxed grains with no apparent elemental segregation. In contrast, the SMC samples reveal compositional heterogeneity across MEA and Fe regions, as illustrated by the corresponding EDS-Fe maps (Fig. 5a_1, b_1, and c_1). These maps distinguish the Fe-rich and Fe-lean regions, indicating that their distinct chemical identities are retained even after annealing. Meanwhile, between the recrystallized MEA region and the Fe region in Figs. 5(a-c), a relatively brighter regions with smaller grain size appears, which are assumed to be the transition region. This transition region shows a blurred Fe distribution at the MEA/Fe interfaces, while the sharper boundaries were observed in the as-HPT samples (Fig. 2). The blurred Fe distribution and finer grain size clearly suggest the different microstructural features of transition region from other regions after annealing.

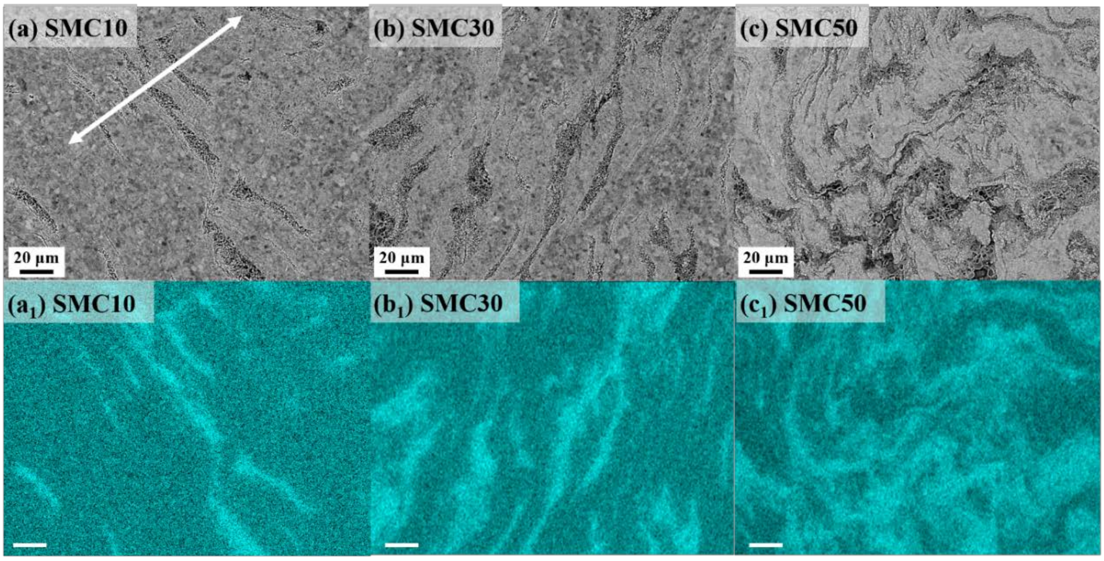

Figure 5. SEM-BSE images of the annealed (a) SMC10, (b) SMC30, and (c) SMC50, along with (1) the corresponding EDS-Fe maps.

EDS line profile was acquired across the regions of the annealed SMC10 sample to assess the compositional gradients in the transition region (Fig. 6). Compared to the as-HPT condition in Fig. 3, the Fe peak intensity is clearly reduced and the compositional gradient region between the MEA and Fe regions has expanded to over 5 μm in width. Expansion of compositionally gradient region suggests that the transition region has grown via substantial atomic interdiffusion during annealing. This observation implies that the transition region is likely to occupy a greater volume fraction in SMC30 and SMC50 samples due to their profuse MEA/Fe interfaces. Point EDS data was obtained in constituent regions (Table 2), which confirms that the Fe content in the MEA region increases after annealing. Therefore, the intensification of FCC instability in MEA regions is expected [8, 16]. Meanwhile, Co, Cr, and Ni are found to diffuse into the Fe region, which is the reason for a decrease in Fe content in Fe regions. Although local composition variations were observed due to the nature of the transition regions, all measurements consistently show intermediate compositions between both MEA and Fe, validating the well-developed transition regions.

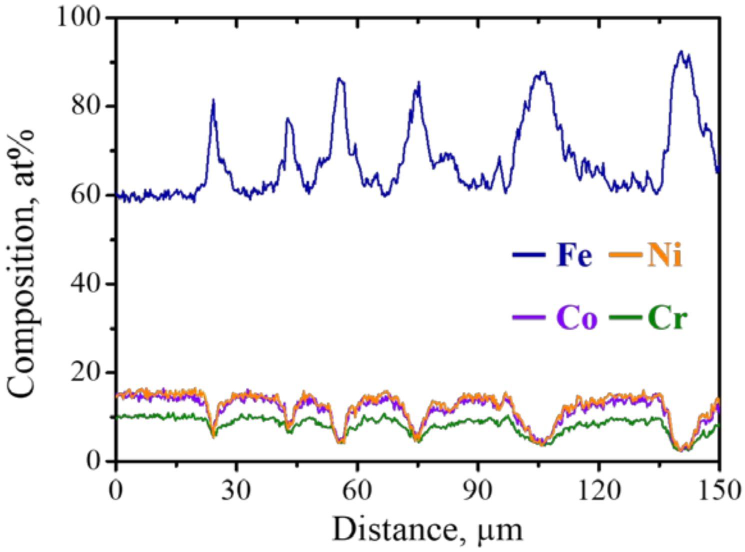

Figure 6. EDS line profiles of the annealed SMC10 obtained from the white line indicated in Fig. 5a.

Table 2. Point EDS obtained from the MEA, Fe, and transition regions in the SMC samples. All EDS values are averaged from more than three points in the corresponding regions.

at%	Region	Co	Cr	Fe	Ni
SMC10	MEA	~14.7	~10.3	~59.5	~15.5
	Fe	~3.9	~3.7	~88.7	~3.7
SMC30	MEA	~14.3	~9.9	~60.8	~15.0
	Transition	~13.1	~8.8	~64.6	~13.5
	Fe	~4.4	~3.9	~88.2	~3.5
SMC50	MEA	~14.2	~9.8	~60.5	~15.5
	Transition	~12.7	~8.8	~65.2	~13.3
	Fe	~1.1	~1.4	~96.6	~0.9

To investigate how compositional changes in each region influenced phase stability, EBSD analysis was conducted. Low-magnification EBSD phase maps were acquired to examine the overall phase distribution (Fig. 7). The annealed ferrous MEA sample was confirmed to consist almost entirely of the FCC phase, with only a small fraction (~0.5 vol%) of BCC detected. In contrast, the SMC samples exhibited a clear increase in the BCC phase fraction with increasing Fe content. The volume fractions of BCC phase in SMC10, SMC30, and SMC50 were quantified as 14.3, 44.2, and 75.1 vol%, respectively, as summarized in Table 3.

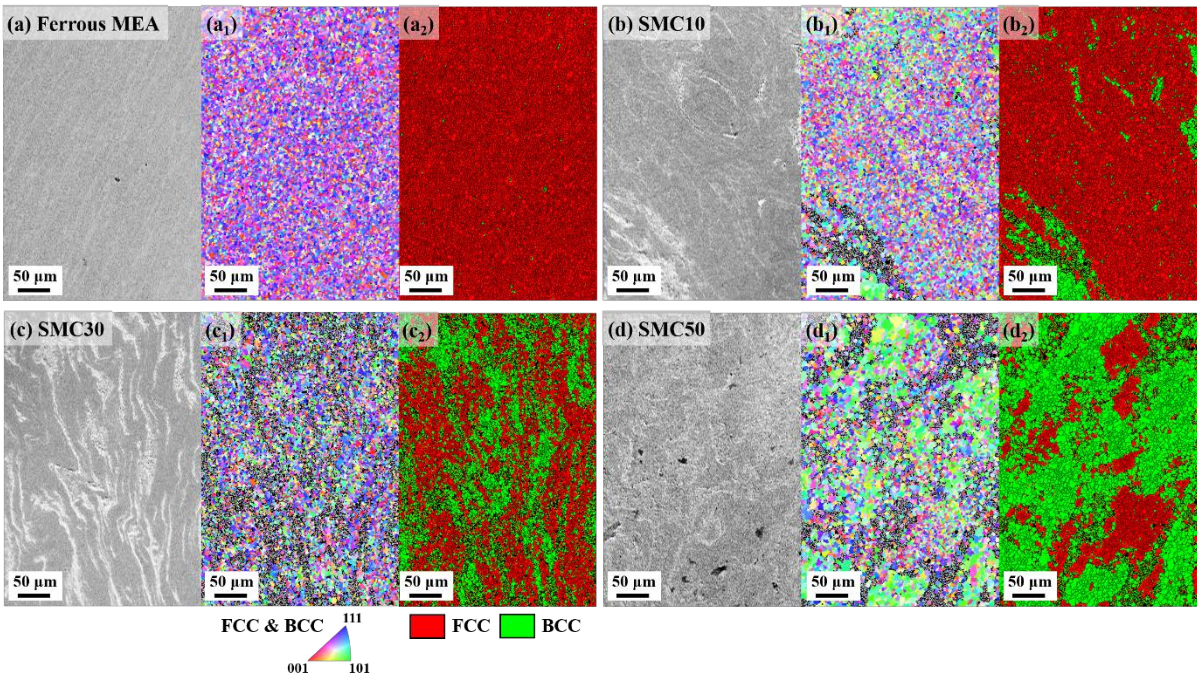

Figure 7. Low magnification microstructures of (a) ferrous MEA, (b) SMC10, (c) SMC30, and (d) SMC50 with (a) EBSD-IPF and (b) EBSD-phase maps.

Table 3. Volume percent of FCC and BCC in the ferrous MEA, SMC10, SMC30, and SMC50, obtained from the EBSD-phase maps in Fig. 7.

vol%	Ferrous MEA	SMC10	SMC30	SMC50
FCC	99.5	85.7	55.8	24.9
BCC	0.5	14.3	44.2	75.1

The BCC fraction exceeds the nominal Fe content in all SMC samples, a trend that is consistent with the XRD results shown in Fig. 4. This suggests that compositional mixing and the presence of a transition region promote additional BCC phase formation beyond what would be expected based on the Fe volume fraction. To figure out the source of increased BCC fraction, EBSD analyses in high-magnification were acquired across the interfaces across the MEA, transition, and Fe regions (Fig. 8). In the annealed ferrous MEA sample (Fig. 8a), a number of annealing twins are observed within equiaxed grains, along with a low fraction of BCC phase. In SMC10 (Fig. 8b), the MEA region also displays multiple annealing twins, proving a low stacking fault energy of the matrix. Due to the relatively low fraction of Fe regions in SMC10, a distinct Fe region is not well defined. The Fe-transition region is better described the regions exhibiting a dual-phase FCC+BCC microstructure. In SMC30 and SMC50, by contrast, the Fe regions are more clearly distinguished. These Fe regions exhibit BCC phase with larger grain size compared to the MEA and transition regions. It is because that the Fe region underwent rapid grain growth during annealing, due to high atomic diffusivity and high grain boundary mobility in low alloyed matrix. In contrast, the finer grain size in the MEA region is consistent with the sluggish diffusion characteristic of HEAs [27, 28]. Meanwhile, the fine grain size in a transition region can be elucidated thermal martensitic transformation [29, 30]. As shown in Figs. 1a and 6, regions with Fe contents exceeding 90 at% lie within the predicted FCC+BCC phase stability range. However, the regions with Fe contents over 90 at% occupied a small portion in transition region. Therefore, it is supposed that during annealing, these regions retained FCC structure but transformed into BCC via thermal martensitic transformation during quenching, as supported by the large $\Delta G^{FCC\rightarrow BCC}$ values at room temperature shown in Fig. 1b. The formation of thermal martensite divided the original FCC grains, leading to finer grains [29, 30].

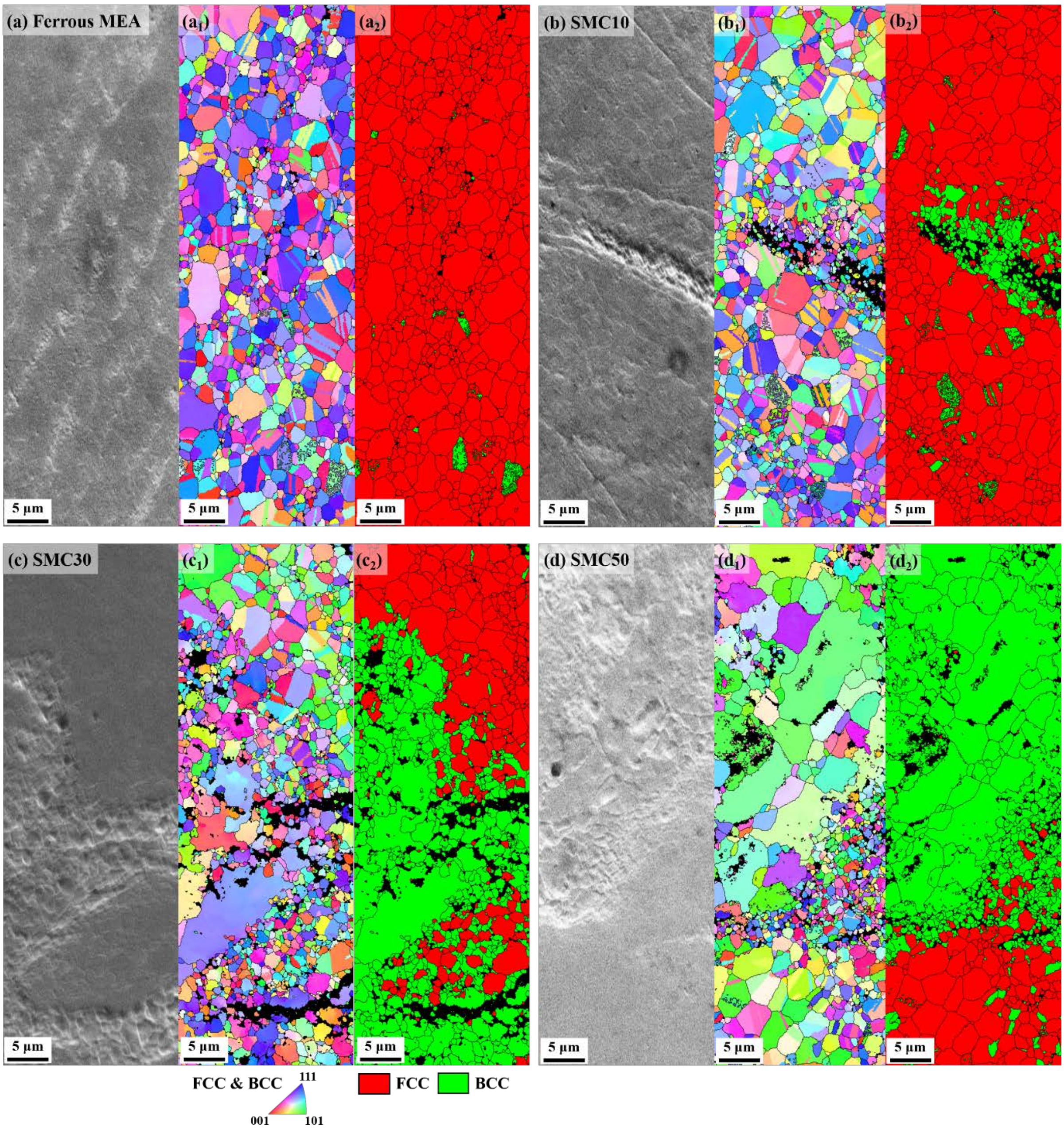

Figure 8. High magnification microstructures of (a) ferrous MEA, (b) SMC10, (c) SMC30, and (d) SMC50 with (a) EBSD-IPF and (b) EBSD-phase maps.

EBSD-KAM maps for SMC50 (Fig. 9) support the formation of thermal martensite in transition regions. While the fully recrystallized MEA and Fe regions show low KAM values, the BCC phase within the transition region exhibits significantly higher KAM values. This suggests that the BCC in the transition region forms via thermal martensitic transformation, characterized by high internal strains, stacking faults, and residual stress [31]. Thus, the BCC phases in the Fe and transition regions have distinct origins and microstructural characteristics.

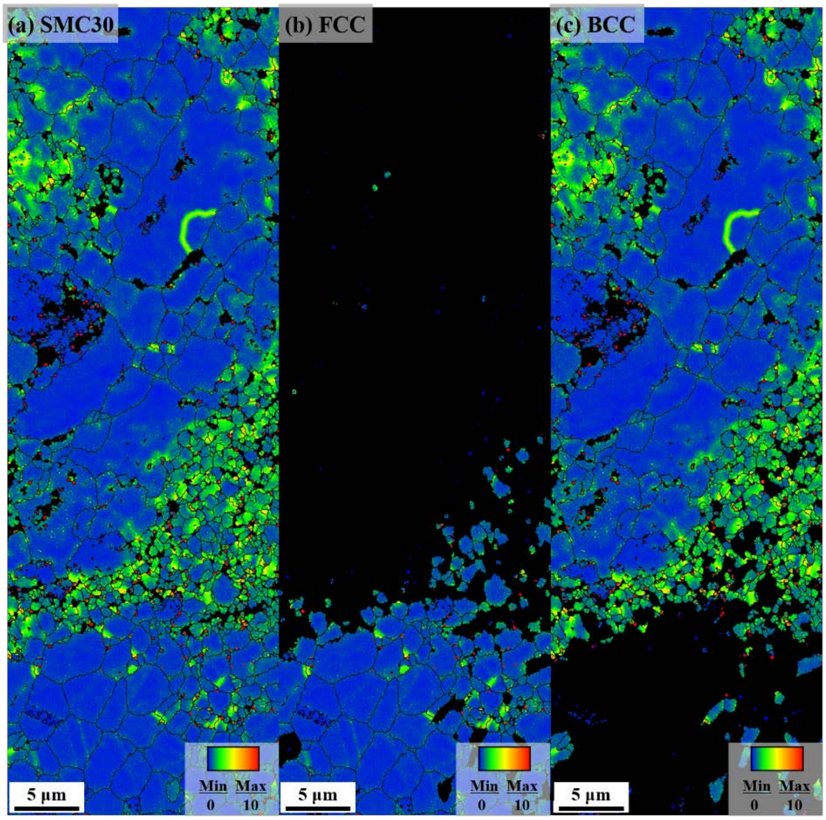

Figure 9. EBSD-KAM maps of SMC50 showing (a) the overall microstructure, (b) FCC phase, and (c) BCC phase.

In Fig. 10, to evaluate the synergistic effect of constituent regions and mechanical behavior of the SMC samples, uniaxial tensile tests were conducted at both room temperature (298 K) and cryogenic temperature (77 K). At 298 K, the annealed ferrous MEA exhibited excellent mechanical properties, with a yield strength (YS) of ~461.1 MPa and a total elongation of ~81.9%. Compared to cast and rolled ferrous MEA samples [8], this represents over a 50% increase in YS with similar ductility. This improvement is attributed to the refined grain structure and residual stress induced by HPT process [14]. The ultimate tensile strength (UTS) also increased to ~624.4 MPa, confirming the superior strength of the HPT-processed ferrous MEA. In the case of the SMC samples, SMC10 exhibited a similar YS of ~463.4 MPa to ferrous MEA, but a higher UTS of ~663.5 MPa, indicating that the enhancement in mechanical performance is mainly driven by increased strain hardening rather than initial yield strength. SMC30 showed a significant improvement in both YS (~582.6 MPa) and UTS (~814.9 MPa), accompanied by a respectable total elongation of ~42.0%. The strain hardening response of SMC30 was particularly notable; although it rapidly reached UTS due to an initial high strain hardening rate (SHR), it maintained substantial ductility thereafter. The SHR curve revealed that unlike the MEA sample, which exhibited an initial drop, SHR recovery and gradual decreasing, SMC10 and SMC30 showed elevated SHR values from the early stages of deformation. However, this high SHR decreased more rapidly in the later stages of deformation, resulting in lower final SHR compared to the MEA.

At 77 K (Figs. 10c, d), the mechanical behavior was remarkably different due to intensified matrix metastability. Fig. 10c presents the plastic region of the cryogenic stress-strain curves. The ferrous MEA showed a dramatic increase in YS (~835.0 MPa) and UTS (~1331.0 MPa), while maintaining a high elongation (~81.6%) attributed to extensive TRIP activity. SMC10 did not exhibit a significant increase of YS (~924.4 MPa) at 77 K compared to ferrous MEA, but showed significantly enhanced UTS (~1464.5 MPa) and a nearly constant high SHR plateau of ~4000 MPa. This is in contrast to the room temperature behavior, where SHR began at ~2000 MPa and declined gradually. The enhanced strain hardening at 77 K is induced by a drastic drop in FCC phase stability, as predicted in Fig. 1b. However, the SHR declined sharply beyond ~25% strain due to depletion of FCC phase, which is the source for phase transformation. SMC30 maintained its high YS (~1107.7 MPa) at 77 K, which is contributed by transition regions providing effective strengthening due to their fine grain size and dual-phase structure. As predicted by the profuse TRIP behavior even at 298 K, SMC30 also showed active TRIP behavior at 77 K resulting in a SHR plateau. However, the plateau value stands ~3000 MPa due to the lower fraction of residual FCC phase. SMC50 showed lower elongation at both temperatures, because SMC50 contained internal pores and was largely composed of relatively brittle BCC phase. Nonetheless, the stress-strain curve of SMC50 revealed a high YS and a strain hardening response at 77 K, indicating the occurrence of TRIP behavior. As the FCC fraction of SMC50 are the smallest (Table 3), TRIP and strain hardening capacities of SMC50 were limited.

Resultantly, these results suggest that SMC30 offers the balanced mechanical performance, successfully overcoming the low yield strength of metastable MEA while retaining substantial ductility. The ability to activate pronounced TRIP behavior even at room temperature through spatial metastability controlling in SMC30 highlights the significance of this multi-material design approach.

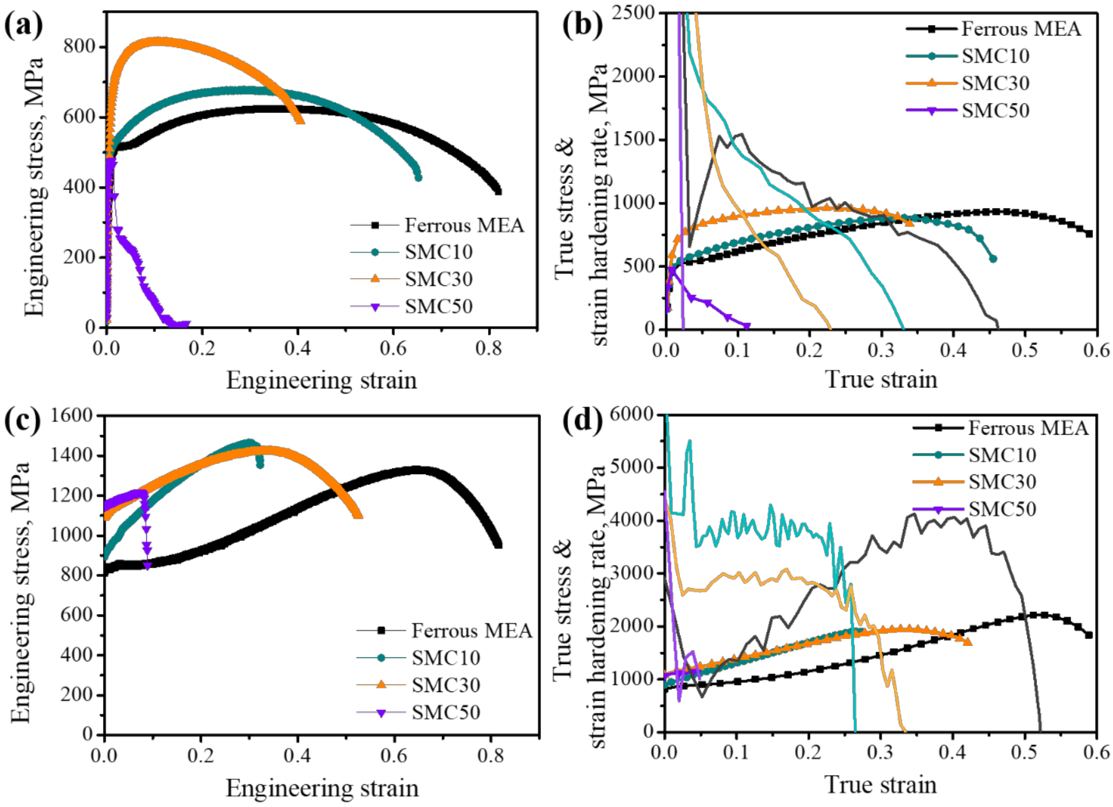

Figure 10. (a, c) Engineering stress-strain curves and (b, d) true stress-strain curves with strain hardening rate curves at (a, b) 298 K and (c, d) 77 K.

To clarify the origin of the mechanical behavior, it is important to define the regions and their characteristics within the SMC structure. The SMC material consists of MEA, pure Fe, transition regions: MEA region with a medium grain size, high solid solution strengthening; pure Fe region with a coarse grain size, low solid solution strengthening; and a transition region between them. At 298 K, pure Fe exhibits low yield strength of ~240 MPa [17], implying that its role is not to act as a reinforcement but rather to modify the deformation mechanisms of the multi-materials. The main contributor to the enhancement of strengths is the transition region, which is the targeted region for spatial metastability control. This region contains thermal martensite with fine grain size and moderate solid solution strengthening, and internal residual stress [32], thus contributing to enhanced strength. Therefore, the transition region is expected to exhibit the highest strength, followed by the MEA and then the pure Fe region.

To verify these predictions, nanoindentation tests were conducted on SMC30. Figure 11a presents representative nanoindentation load-displacement (P-h) curves for each region. Figure 11b summarizes the corresponding hardness values, which were obtained using the CSM method as a function of depth and averaged over the stable range above 80% of P_{max} [33]. When compared to bulk hardness values, pure Fe (102 Hv [34]) exhibits a lower hardness than Co (166 Hv [35]), Cr (200 Hv [36]), and Ni (110 Hv [37]). Accordingly, the MEA composed with these elements is expected to have a higher hardness than Fe, with the rule of mixtures predicting ~123 Hv. The transition region, based only on composition, would be expected to exhibit an intermediate hardness value between those of MEA and pure Fe. However, the nanoindentation results revealed hardness values of 2.52 ± 0.22, 2.33 ± 0.63, and 4.88 ± 0.50 GPa for the MEA, Fe, and transition regions, respectively. As expected, the MEA region exhibits a higher hardness than Fe. However, the transition region shows the higher hardness, surpassing compositional expectations. This enhanced hardness is attributed to grain refinement by thermal martensitic transformation during quenching, with moderate solid-solution strengthening and residual stresses, which provide additional hardening beyond compositional effects.

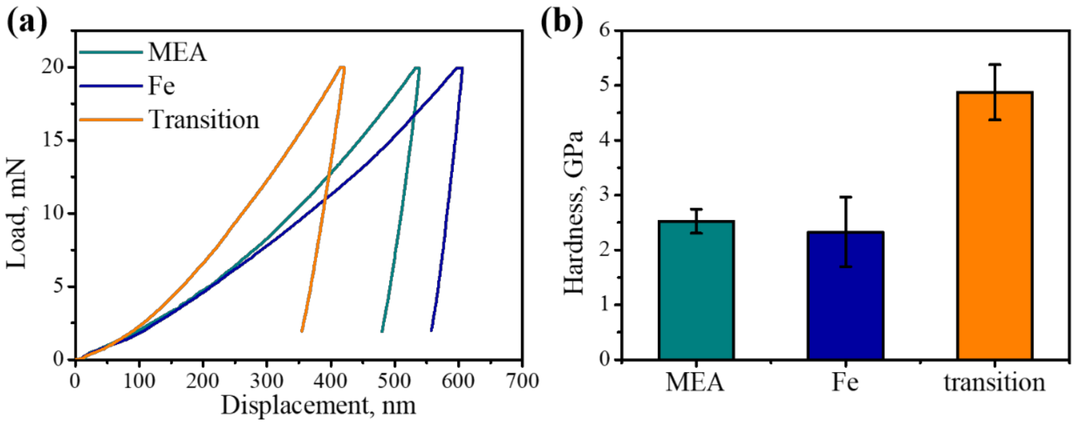

Figure 11. Nanoindentation test results of MEA, Fe, and transition regions in the SMC30; (a) Representative load-displacement curves and (b) hardness values.

The deformed microstructures of the SMC30 were compared with the deformed microstructure of the ferrous MEA after tensile test at 298 K (Fig. 12). The local strain in each region was evaluated using DIC strain maps, allowing for microstructural analysis at various deformation levels. At a local strain (ε_{local}) of 0.45 in the ferrous MEA (Fig. 12a), the BCC phase fraction ended up only to 22.6 vol%. The average KAM values for FCC and BCC phases in this condition were 1.44^o and 1.33^o, respectively. In contrast, SMC30 showed a BCC phase fraction started from 44.2 vol% at initial microstructure and increased with further deformation. At ε_{local}= 0.05 (Fig. 12b), TRIP had already initiated in both the transition and MEA regions. The KAM maps showed average values of 0.46^o for FCC and 2.02^o for BCC, suggesting that most of the plastic deformation proceeded by BCC transformation. At ε_{local}=0.18 (Fig. 12c), corresponding to the peak in strain hardening rate, most of the MEA region had transformed to BCC, with only a small fraction of FCC remaining. The KAM values at this stage were 0.72^o for FCC and 2.18^o for BCC, indicating that the majority of the deformation was still accommodated by the TRIP behavior. However, at ε_{local}=0.35 (Fig. 12d), where the SHR significantly decreased, the BCC fraction in the MEA region did not increase substantially. Instead, the FCC phase exhibited a sharply increased KAM value of 2.10^o, and the BCC phase also showed a higher KAM of 3.09^o. This suggests that while deformation via phase transformation dominated during the earlier stages of deformation up to the SHR peak, strain hardening after SHR peak was governed by dislocation accumulation. Consequently, the overall hardening capability diminished, leading to the observed drop in SHR.

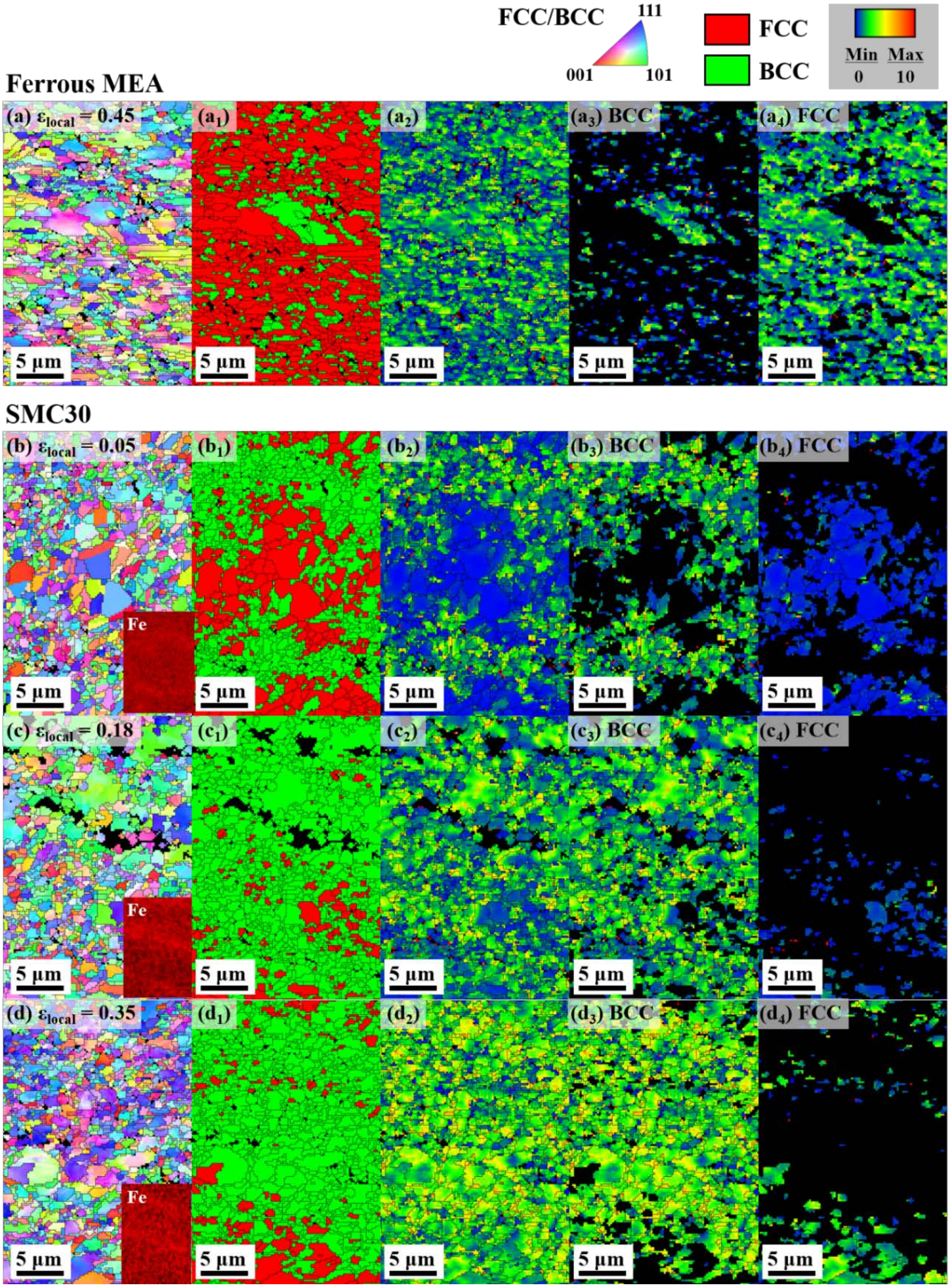

Figure 12. EBSD-IPF maps with (1) EBSD-phase, (2-4) EBSD-KAM maps of the (a) ferrous MEA and (b-d) SMC30 samples deformed at 298 K. The deformed microstructures of SMC30

at various local strains of (b) 0.05, (c) 0.18, and (d) 0.35 were identified using DIC strain mapping. Fe elemental distribution maps of SMC30 samples are shown as insets in (b-d). (2) The overall KAM maps are further separated into (3) BCC-KAM and (4) FCC-KAM maps. The KAM maps are measured up to the third nearest neighbor with a maximum misorientation of 10°.

Although the absence of DIC in cryogenic specimens made it difficult to precisely evaluate local strain, the uniformly deformed region was assumed to represent the deformed microstructure at UTS for microstructural analysis. At 77 K, the difference from 298 K was the high yield strength of pure Fe over 700 MPa [17], which can be attributed the strong temperature dependency of Peierls potential of screw dislocation in BCC structure [38]. While YS of pure Fe is expected to improve after HPT process, its inherent brittleness under cryogenic conditions resulted in early fracture. In the uniformly deformed region of ferrous MEA (Fig. 13a), 74.6 vol% of the FCC phase had transformed into BCC. Given that previous studies reported ~50 vol% transformation prior to the SHR peak [8], the observed volume fraction of BCC seems to be consistent with TRIP progress at the SHR peak. In comparison, SMC30 exhibited 97.0 vol% BCC in the same uniformly deformed region in Fig. 13b. Excluding the contribution of initially present BCC, ~95.0 vol% of the FCC phase had undergone transformation, which is substantially higher than in ferrous MEA. This accelerated phase transformation is attributed not only to the controlled reduction in FCC stability via Fe diffusion, but also to strain partitioning [39, 40]: the relatively hard martensite region imposed additional strain on the surrounding softer MEA matrix, further promoting TRIP. Thus, the combination of spatially controlled metastability and heterostructure-driven strain localization served to accelerate transformation kinetics and improve mechanical performance.

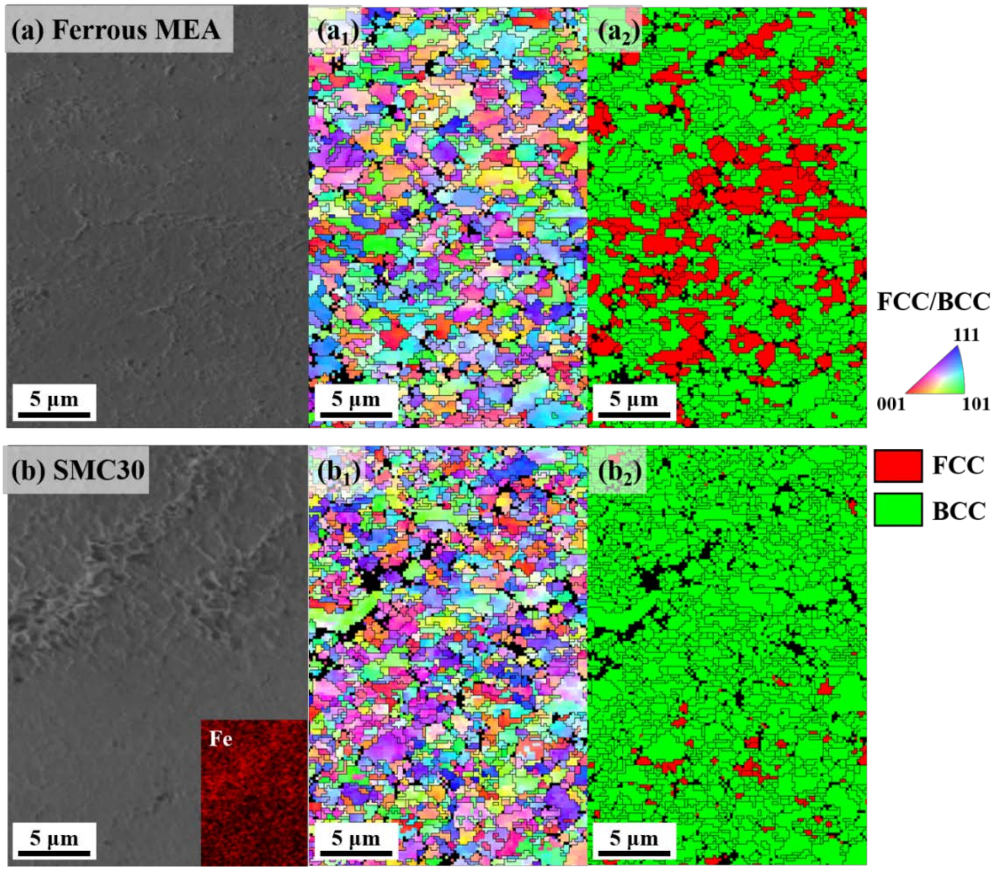

Figure 13. SEM micrographs with corresponding (1) EBSD-IPF and (2) EBSD-Phase maps of the (a) ferrous MEA and (b) SMC30 samples deformed at 77 K. Fe elemental distribution map of SMC30 sample is shown as an inset in (b). The KAM maps were calculated up to the third nearest neighbor with a maximum misorientation of 10°.

In general, heterogeneous materials tend to exhibit stress concentrations at the interface between two distinct regions. However, in the SMC multi-materials, the transition region is the strongest among the three constituent regions. Additionally, strong bonding across the MEA-Fe regions achieved by HPT process, avoiding significant interfacial delamination. As a result, the SMC samples predominantly exhibited ductile fracture (Fig. 14). In contrast, SMC50 displayed signs of interfacial delamination (Fig. 14c), with thin strip-like regions peeling and fracturing in a layered manner. This fracture mechanism is likely responsible for the significantly reduced elongation observed in SMC50.

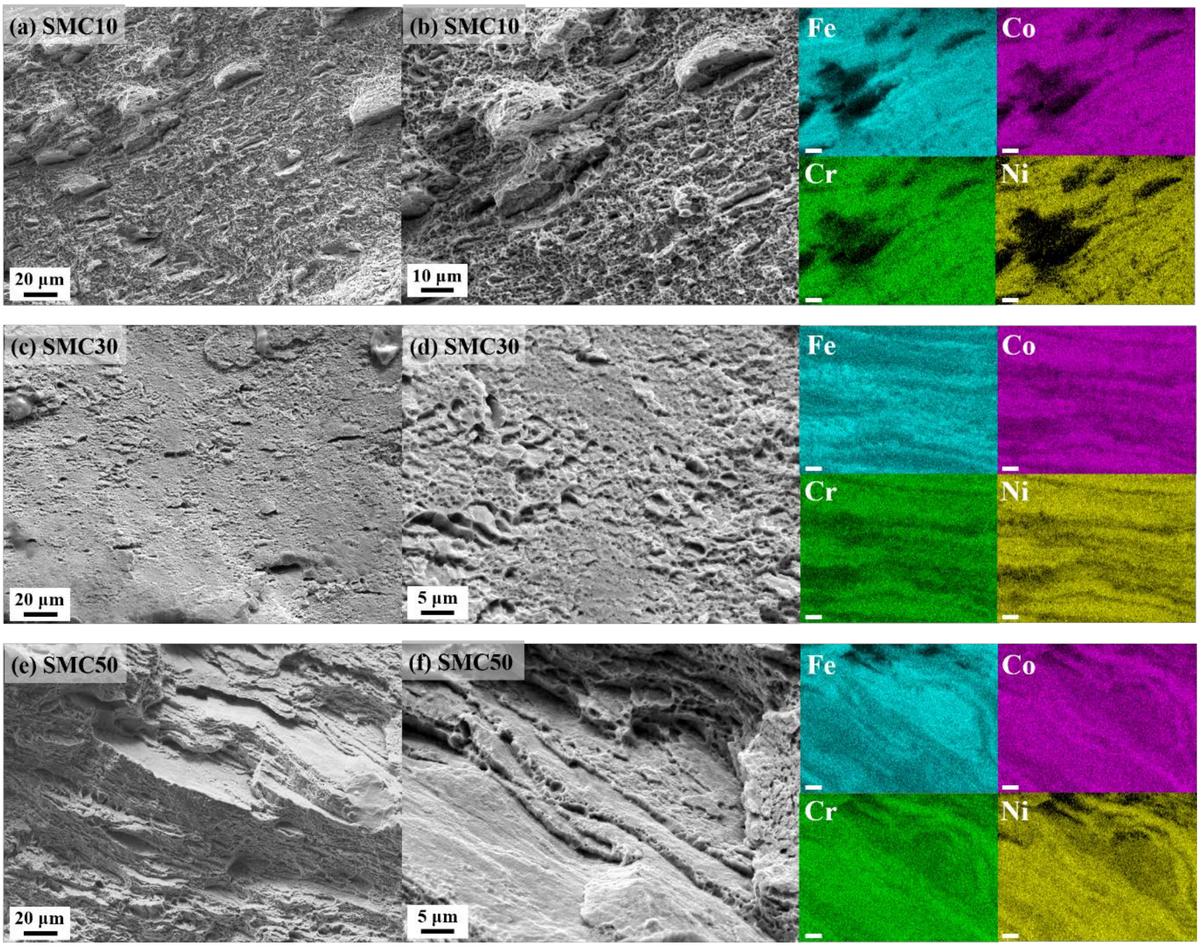

Figure 14. (a, c, e) Fracture surfaces of SMC samples and (b, d, f) fracture morphologies with corresponding EDS maps after tensile test at 77 K.

Figure 15 shows the schematic for the microstructural evolution of SMC multi-materials from the fabrication to deformed microstructures. The as-HPT bulk disk was fabricated from the MEA and Fe powders. Between two domains, the narrow transition region was initially formed by mechanical mixing under the severe friction stress of the HPT process. Subsequent annealing promoted thermal diffusion across the interface, thereby widening the transition region. After water quenching, three distinct regions were distinguished: the MEA region with metastable FCC structure, the Fe region with a stable BCC structure, and a transition region containing thermal martensite within FCC matrix. Upon tensile deformation at 298 K and 77 K, sequential TRIP activation occurred, initiating from FCC phase with higher Fe content to FCC phases with lower Fe content. At both temperature, FCC to BCC phase transformation was nearly completed in the transition region. In addition, the strain partitioning and the mixed composition within MEA regions promoted profuse TRIP behavior, resulting in an increased phase-transformation fraction and enhanced strain hardening as well as overall mechanical performance.

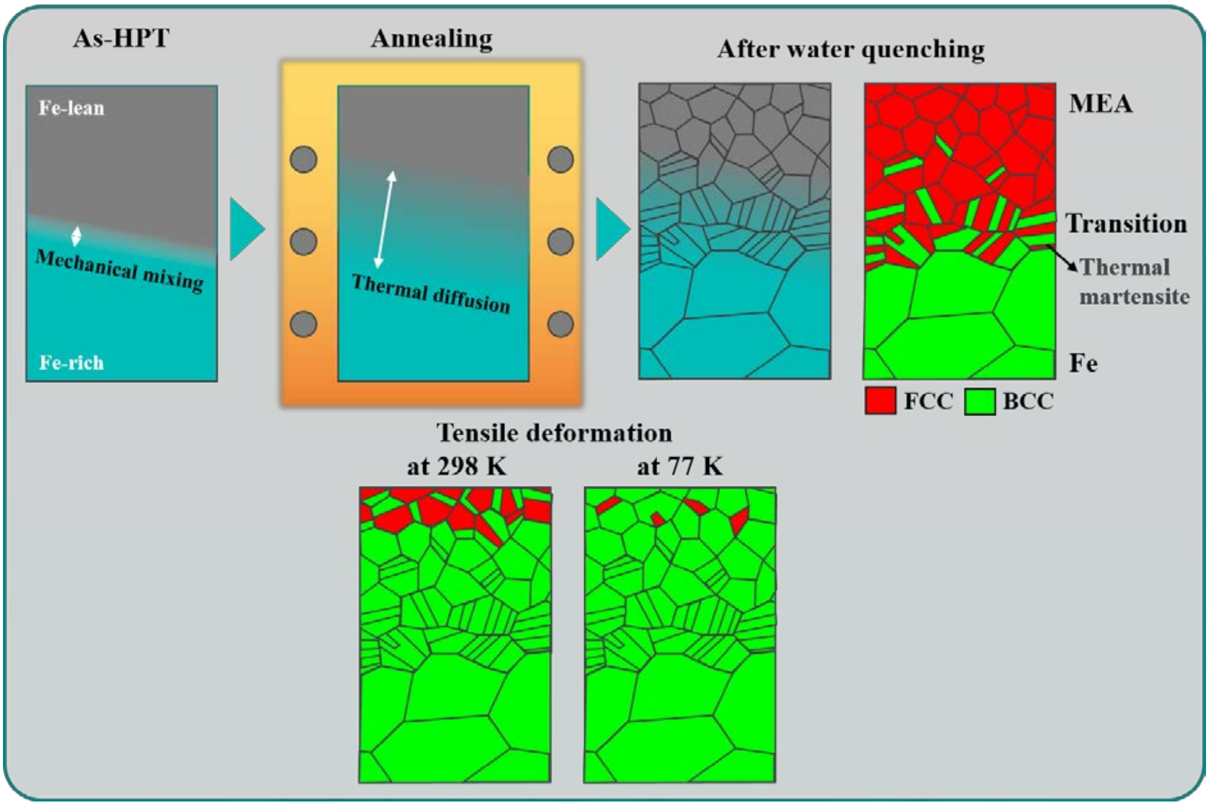

Figure 15. Schematic illustration of the microstructural evolution in SMC multi-materials.

4. Conclusion

In this study, we proposed a novel strategy for controlling matrix metastability in ferrous MEA through a multi-material design incorporating pure Fe. This approach, referred to as SMC design, enables partial tuning of the FCC matrix stability by introducing compositional gradients at the MEA/Fe interface. The resulting transition region, formed between the MEA and pure Fe regions, emerges as a key microstructural feature due to its unique combination of thermal martensite, moderate solid solution strengthening, and refined grain size. This region not only contributes significantly to overall strength but also acts as a preferential site for TRIP activation. As a result, SMC30 exhibited the most outstanding mechanical properties at 298 K, with a yield strength of ~582.6 MPa and a tensile strength of ~814.9 MPa, demonstrating that TRIP can be efficiently activated even at room temperature by engineering local stability variations. At 77 K, SMC30 achieved high YS of ~1107.7 MPa and UTS of ~1423.3 MPa. High BCC volume fraction of 95 vol% in the SMC30 deformed at 77 K insists effectiveness of spatially controlled metastability and strain partitioning mechanisms in promoting TRIP. Furthermore, diverse scalable processing routes such as sintering, hot isostatic pressing, and additive manufacturing can realize the SMC strategy by forming transition regions through powder mixing and thermal diffusion. This underscores the potential of the SMC design as a promising pathway toward the development of high-performance structural materials capable of maintaining superior mechanical behavior across a wide temperature range.

Declaration

Authors' contributions

Design: Son S.

Experiments and data collection: Son S., Ha H, Ha S.V. Lee S.W., Koo B.W., Gao Z., Jang J.-I.

Software: Lee J.-S., Lee B.-J.

Data analysis: Son S., Lee S.W.

Manuscript writing: Son S.

Manuscript revision and supervising: Kim H.S.

All authors have read and agreed to the published version of the manuscript.

Availability of data and materials

The raw data supporting the findings of this study are available within this Article and its Supplementary Materials. Further data is available from the corresponding authors upon reasonable request.

Acknowledgments

This work was supported by National Research Foundation of Korea (NRF) (RS-2023-00281246).

Conflict of Interests

The authors declare no conflicts of interest.

Ethical approval and consent to participate

Not applicable.

Consent for publication

Not applicable.

Copyright

References

[1] Zhu, Y.T., Ameyama, K., Anderson, P.M., Beyerlein, I.J., Gao, H.J., Kim, H.S., et al. Heterostructured materials: superior properties from hetero-zone interaction. Mater. Res. Lett. 2021, 9, 1-31. https://doi.org/10.1080/21663831.2020.1796836.

[2] Wu, D., Hao, M.Y., Zhang, T.L., Wang, Z., Wang, J., Rao, G.H., et al. Heterostructures enhance simultaneously strength and ductility of a commercial titanium alloy. Acta Mater. 2023, 257, 119182. https://doi.org/10.1016/j.actamat.2023.119182.

[3] Ying, H., Yang, X., He, H., Tao, K., Guo, Z., Wang, L., Ge, J., Liu, S., Fu, S., Lou, Y., He, L., Ren, Y., Zhu, H., Wu, Z., Lan, S., Formation of strong and ductile FeNiCoCrB networkstructured high-entropy alloys by fluxing, Microstructures 2023, 3, 2023018. DOI: 10.20517/microstructures.2022.47.

[4] Son, S., Lee, J.W., Asghari-Rad, P., Kim, R.E., Park, H., Jang, J.I., et al. Hierarchically heterogeneous microstructure and mechanical behavior of the multi-materials prepared by powder severe plastic deformation. Mater. Res. Lett. 2023, 11(11), 915-924. https://doi.org/10.1080/21663831.2023.2258158.

[5] Wu, W.T., Fu, H., Xia, P., Gan, B., Jiang, N.S., Xia, M., et al. Heterogeneous Microstructure Evolution and Mechanical Properties of a CrCoNiAl1Ti2 Medium-Entropy Alloy by Thermo-Mechanical Treatment. Met. Mater. Int. 2024, 31, 1613-1626. https://doi.org/10.1007/s12540-024-01845-z.

[6] Cao, P.L., Li, C.B., Zhu, D.B., Zhao, C., Xiao, B., Zhang, X.M. Heterogeneous Precipitation Behavior of 7085 Aluminum Alloy was Studied by High-Throughput Experiment Based on End-Quenching Technology. Met. Mater. Int. 2024, 30, 1965-76. https://doi.org/10.1007/s12540-024-01627-7.

[7] Wang, Y.F., Ma, X.L., Guo, F.J., Zhao, Z.F., Huang, C.X., Zhu, Y.T., et al. Strong and ductile CrCoNi medium-entropy alloy via dispersed heterostructure. Mater. Des. 2023, 225, 111593. https://doi.org/10.1016/j.matdes.2023.111593.

[8] Bae, J.W., Seol, J.B., Moon, J., Sohn, S.S., Jang, M.J., Um, H.Y., et al. Exceptional phase-transformation strengthening of ferrous medium entropy alloys at cryogenic temperatures. Acta Mater. 2018, 161, 388-99. https://doi.org/10.1016/j.actamat.2018.09.057.

[9] Li, Z.M., Pradeep, K.G., Deng, Y., Raabe, D., Tasan, C.C. Metastable high-entropy dual-phase alloys overcome the strength-ductility trade-off. Nature 2016, 534, 227-230. https://doi.org/10.1038/nature17981.

[10] Astafurova, E., Astafurov, S., Luchin, A., Gurtova, D., Melnikov, E., Sanin, V. A comparative study of metastability-driven and twinning-assisted hardening in Fe40Mn40Co10Cr10 and FeMnCoCrNi multi-principal element alloys in cold rolling. Mater. Lett. 2024, 373, 137175. https://doi.org/10.1016/j.matlet.2024.137175.

[11] Guoa, S.K., Ma, Z., Xiaa, G.H., Li, X.Y., Xua, Z.Q., Li, W., et al. Pursuing ultrastrong and ductile medium entropy alloys via architecting nanoprecipitates-enhanced hierarchical heterostructure. Acta Mater. 2024, 263, 119492. https://doi.org/10.1016/j.actamat.2023.119492.

[12] Zhao, J., Zhang, J., Li, X., Gao, X., Guo, N., Shi, C., et al. Microstructure evolution and strengthening mechanism of AlCrFe2NiCuMox high entropy alloys, Met. Mater. Int. 30 (2024) 3005-3013. https://doi.org/10.1007/s12540-024-01687-9.

[13] Dewangan, S.K., Jain, R., Paswan, M., Patel, A., Samal, S., Kumar, V., et al. Exploring Zr Influence on Microstructure and Mechanical Property in FeCoNiCrCuZr Eutectic High-Entropy Alloys. Met. Mater. Int. 2024, 30, 3339-3348. https://doi.org/10.1007/s12540-024-01716-7.

[14] Zhang, Z.Q., Fellner, S., Hohenwarter, A., Renk, O., Huang, Y., Chen, Z., et al. Microstructure evolution and mechanical properties of a lamellar AlCoCrFeNi2.1 eutectic high-entropy alloy processed by high-pressure torsion. Mater. Sci. Eng. A 2024, 914, 147139. https://doi.org/10.1016/j.msea.2024.147139.

[15] Asghari-Rad, P., Kim, Y., Gu, G.H., Kato, H., Kim, H.S. Exploring the impact of hard-to-soft domain ratios in a heterostructured multi-principal element alloy. Mater. Sci. Eng. A 2025, 927, 148024. https://doi.org/10.1016/j.msea.2025.148024.

[16] Choi, Y.T., Kwon, J., Kim, R.E., Lee, S.Y., Lee, D.W., Kim, J., et al. Effects of deformation-induced BCC martensitic transformation on uniaxial ductility and biaxial

stretchability in metastable ferrous medium-entropy alloys. Mater. Sci. Eng. A 2024, 913, 147065. https://doi.org/10.1016/j.msea.2024.147065.

[17] Koga, N., Tomono, S., Umezawa, O. Low-temperature tensile properties of Cu-Fe laminated sheets with various number of layers. Mat. Sci. Eng. A 2021, 811, 141066. https://doi.org/10.1016/j.msea.2021.141066.

[18] Castro, M.M., Montoro, L.A., Isaac, A., Kawasaki, M., Figueiredo, R.B. Mechanical mixing of Mg and Zn using high-pressure torsion. J. Alloy Compd. 2021, 869, 159302. https://doi.org/10.1016/j.jallcom.2021.159302.

[19] Mazilkin, A., Tavakkoli, V., Davydenko, O., Beygelzimer, Y., Boltynjuk, E., Boll, T., et al. Mechanisms of structural evolution of laminates with immiscible components under high-pressure torsion. Acta Mater. 2024, 269, 119804. https://doi.org/10.1016/j.actamat.2024.119804.

[20] Asghari-Rad, P., Sathiyamoorthi, P., Nguyen, N.T.C., Zargaran, A., Kim, T.S., Kim, H.S. A powder-metallurgy-based fabrication route towards achieving high tensile strength with ultra-high ductility in high-entropy alloy. Scr. Mater. 2021, 190, 69-74. https://doi.org/10.1016/j.scriptamat.2020.08.038.

[21] Y. Beygelzimer, Y. Estrin, A. Mazilkin, T. Scherer, B. Baretzky, H. Hahn, R. Kulagin, Quantifying solid-state mechanical mixing by high-pressure torsion, J. Alloy Compd. 878 (2021) 160419. https://doi.org/10.1016/j.jallcom.2021.160419.

[22] Y. Beygelzimer, R. Kulagin, P. Fratzl, Y. Estrin, The earth’s lithosphere inspires materials design, Adv. Mater. 33 (2021) 2005473. https://doi.org/10.1002/adma.202005473.

[23] A. Kilmametov, R. Kulagin, S. Seils, T. Boll, M. Heilmaier, H. Hahn, High-pressure torsion driven mechanical alloying of CoCrFeMnNi high entropy alloy, Scr. Mater. 158 (2019) 29-33. https://doi.org/10.1016/j.scriptamat.2018.08.031.

[24] J.-K. Han, T. Herndon, J.-I. Jang, T.G. Langdon, M. Kawasaki, Synthesis of hybrid nanocrystalline alloys by mechanical bonding through high-pressure torsion, Adv. Eng. Mater. 22 (2020) 1901289. https://doi.org/10.1002/adem.201901289.

[25] A. Bachmaier, M. Kerber, D. Setman, R. Pippan, The formation of supersaturated solid solutions in Fe–Cu alloys deformed by high-pressure torsion, Acta Mater. 60 (2012) 860-871. https://doi.org/10.1016/j.actamat.2011.10.044.

[26] Kang, J.Y., Kim, J.G., Kim, S.K., Chin, K.G., Lee, S., Kim, H.S. Outstanding mechanical properties of high-pressure torsion processed multiscale TWIP-cored three layer steel sheet. Scr. Mater. 2016, 123, 122-125. https://doi.org/10.1016/j.scriptamat.2016.06.009.

[27] Tsai, K.Y., Tsai, M.H., Yeh, J.W. Sluggish diffusion in Co-Cr-Fe-Mn-Ni high-entropy alloys. Acta Mater. 2013, 61, 4887-4897. https://doi.org/10.1016/j.actamat.2013.04.058.

[28] Mehta, A., Sohn, Y. High Entropy and Sluggish Diffusion "Core" Effects in Senary FCC Al-Co-Cr-Fe-Ni-Mn Alloys. ACS Comb. Sci. 2020, 22, 757-767. https://doi.org/10.1021/acscombsci.0c00096.

[29] Su, J., Raabe, D., Li, Z.M. Hierarchical microstructure design to tune the mechanical behavior of an interstitial TRIP-TWIP high-entropy alloy. Acta Mater. 2019, 163, 40-54. https://doi.org/10.1016/j.actamat.2018.10.017.

[30] Dirras, G., Tingaud, D., Ueda, D., Hocini, A., Ameyama, K. Dynamic Hall-Petch versus grain-size gradient effects on the mechanical behavior under simple shear loading of 13-titanium Ti-25Nb-25Zr alloys. Mater. Lett. 2017, 206, 214-216. https://doi.org/10.1016/j.matlet.2017.07.027.

[31] Hidalgo, J., Findley, K.O., Santofimia, M.J. Thermal and mechanical stability of retained austenite surrounded by martensite with different degrees of tempering. Mater. Sci. Eng. A 2017, 690, 337-347. https://doi.org/10.1016/j.msea.2017.03.017.

[32] Fukui, D., Nakada, N., Onaka, S. Internal residual stress originated from Bain strain and its effect on hardness in Fe-Ni martensite. Acta Mater. 2020, 196, 660-668. https://doi.org/10.1016/j.actamat.2020.07.013.

[33] Akbarzadeh, E., Yurtisik, K., Hakan Gur, C., Saeid, T., Tavangar, R., Influence of Shielding Gas on the Microstructure and Mechanical Properties of Duplex Stainless Steel in Wire Arc Additive Manufacturing, Met. Mater. Int. 30 (2024) 1977-1996. https://doi.org/10.1007/s12540-023-01623-3.

[34] Zhang, Y., Zhang, K., Liu, W., Zheng, Z., Zhao, M., Grain growth upon annealing and its influence on biodegradation rate for pure iron, Materials 15 (2022) 8030. https://doi.org/10.3390/ma15228030.

[35] Cipres, V.C., Garcia, J., Cabrera, J.M., Lanes, L., Hot deformation behaviour of sintered cobalt, J. Mater. Res. Technol. 27 (2023) 6513-6526. https://doi.org/10.1016/j.jmrt.2023.10.291.

[36] Kim, Y.S., Gokcekaya, O., Matsugaki, A., Nakano, T., Effect of laser scan speed on defects and texture development of pure Chromium metal fabricated via powder bed fusion-laser beam, Materials 27 (2024) 2097. https://doi.org/10.3390/ma17092097.

[37] Sun, M., Ding, C., Xu, J., Shan, D., Guo, B., Langdon, T.G., Microhardness and microstructural evolution of pure nickel processed by high-pressure torsion, Crystals 13 (2023) 887. https://doi.org/10.3390/cryst13060887.

[38] Kuramoto, E., Aono, Y., Kitajima, K. Thermally activated slip deformation of high purity iron single crystals between 4.2 K and 300 K. Scr. Metall. 1979, 13, 1039-1042. https://doi.org/10.1016/0036-9748(79)90199-6.

[39] Pelligra, C., Samei, J., Amirkhiz, B.S., Hector, L.J.r., Wilkinson, D.S. Microstrain partitioning, Transformation Induced Plasticity, and the evolution of damage during deformation of an austenitic-martensitic 1.5 GPa Quench and Partition steel. Mater. Sci. Eng. A 2024, 895, 146181. https://doi.org/10.1016/j.msea.2024.146181.

[40] Tan, X.D., Ponge, D., Lu, W.J., Xu, Y.B., He, H.S., Yan, J., et al. Joint investigation of strain partitioning and chemical partitioning in ferrite-containing TRIP-assisted steels. Acta Mater. 2020, 186, 374-388. https://doi.org/10.1016/j.actamat.2019.12.050.